Noninvasive Estimation of the Input Function for Dynamic Mouse ^{18}F-FDG MicroPET Studies

Wei Mu, Zhe Chen, Xiaoqian Dai, and Jie Tian*, *Fellow, IEEE*

***Abstract*—A new noninvasive estimation method for the plasma time-activity curve, i.e., input function (IF) of the tracer kinetic model in dynamic ^{18}F-FDG microPET mouse studies, is proposed and validated. This estimation method comprises of four steps. First, a novel constraint nonnegative matrix factorization segmentation algorithm was applied to extract the left ventricle (Lv) and myocardium (Myo) time activity curves (TACs). Second, we modeled the IF as a seven-parameter mathematical equation and constructed a dual-output model of the real TAC in Lv and Myo accounting for the partial-volume and spillover effects. Then, we fit the image-derived Lv and Myo TACs to the dual-output model to estimate the parameters of the IF. Finally, the IF was validated by comparing it to the gold standard IF while considering the delay and dispersion effects. Our method was verified based on 20 mice datasets from the Mouse Quantitation Program database, provided by UCLA. The error of the areas under the curves between the delayed and dispersed estimated IF and the gold standard IF was $7.237\% \pm 6.742\%$ ($r = 0.969$), and the error of the ^{18}F-FDG influx constant Ki of the Myo was $4.910\% \pm 6.810\%$ ($r = 0.992$). The results demonstrated the effectiveness of the proposed method.**

***Index Terms*—Bayesian penalty term, constraint nonnegative matrix factorization (CNMF), delay and dispersion effects, input function, partial-volume and spillover effects.**

I. Introduction

THE tracer kinetic modeling techniques are widely applied in positron emission tomography (PET) ^{18}F-FDG imaging for the quantitative glucose metabolism estimation, in which the ^{18}F-FDG plasma time-activity curve (PTAC) and tissue time-activity curve (TTAC) are required as the input function (IF) and output function (OF) to fit certain tracer kinetic model parameters, i.e., the meaningful physiological parameters. Typically, to obtain the gold standard of the IF, the radioactivity of the arterial plasma samples is measured by the insertion of the catheter into the arterial lines with subsequent collections. However, it is invasive, which limits its routine use in research, especially for small animals such as in mouse studies because of the small size of blood vessels and the limited blood volume [1]. Many alternative methods to estimate the IF noninvasively have been proposed as a result. Those methods can be divided into four categories. The first approach extracts the IF from the image by drawing regions of interest (ROIs) over the major vascular structures [2], [3], such as the left ventricle (Lv) and the abdominal aorta, whereas this method was more challenging by using a mouse due to the small size of the mouse and partial-volume and spillover effects. The second approach standardizes the IF over a large population under the assumption that the individual IF has an identical curve shape and can be approximated by scaling the standard IF to a proper scale with one or two blood samples [4]. However, this method does not account for the variety of curve shapes and has not been validated for small animals, which influences its accuracy. The third approach attempts to extract the IF using a statistical analysis, such as the factor analysis [5] and independent component analysis (ICA) [6]–[8], while the extracted blood vessel component that reveals the IF cannot completely eliminate the spillover and partial-volume effects, especially for mice. The fourth approach models the IF by a mathematical equation, whose parameters can be simultaneously estimated by fitting the IF to several specific organs data [1], [9]. So far, this method gives the most accurate results, but requires two or three late blood samples in the fitting process.

In this study, we proposed and validated a novel noninvasive method that belongs to the fourth approach. The proposed method consisted of four major steps (shown in Fig. 1): first, extract TACs of Lv, myocardium (Myo) and liver; second, model the IF and OFs by taking into account the partial-volume and spillover effects; third, construct the objective function and simultaneously estimate the IF and OFs parameters; finally, validate the estimated IF compared with gold standard IF based on the consideration of the delay and dispersion effects. In step 1, a constraint nonnegative matrix factorization (CNMF)-based method was proposed to automatically extract TACs of Lv and Myo since it is difficult and complicated to draw their ROIs manually. The partial-volume and spillover effects were corrected in step 2 by introducing two mixing coefficients and modeling the outputs of Lv and Myo as a linear combination of blood

Manuscript received February 8, 2013; revised May 9, 2013; accepted June 3, 2013. Date of publication June 19, 2013; date of current version October 16, 2013. This work was supported in part by the National Basic Research Program of China (973 Program) under Grant 2011CB707700, in part by the Instrument Developing Project of the Chinese Academy of Sciences under Grant YZ201164, in part by the National Natural Science Foundation of China under Grant 81227901, Grant 61231004, Grant 81027002, Grant 81071205, Grant 81071129, Grant 81101095, in part by the National Key Technology R&D Program under Grant 2012BAI23B01, Grant 2012BAI23B06, in part by the Beijing Natural Science Foundation under Grant 4111004, in part by the Fellowship for Young International Scientists of the Chinese Academy of Sciences under Grant 2010Y2GA03, in part by the Chinese Academy of Sciences Visiting Professorship for Senior International Scientists under Grant 2012T1G0036, Grant 2010T2G36, Grant 2012T1G0039, and in part by the NSFC-NIH Biomedical collaborative research program under Grant 81261120414. *Asterisk indicates corresponding author.*

W. Mu, Z. Chen, and X. Dai are with the Key Laboratory of Molecular Imaging and Functional Imaging, Institute of Automation, Chinese Academy of Sciences, Beijing 100190, China (e-mail: wei.mu@ia.ac.cn; zhe.chen@siemens.com; daixq.casia@gmail.com).

*J. Tian is with the Key Laboratory of Molecular Imaging and Functional Imaging, Institute of Automation, Chinese Academy of Sciences, Beijing 100190, China (e-mail: tian@ieee.org).

Color versions of one or more of the figures in this paper are available online at http://ieeexplore.ieee.org.

Digital Object Identifier 10.1109/TBME.2013.2267778

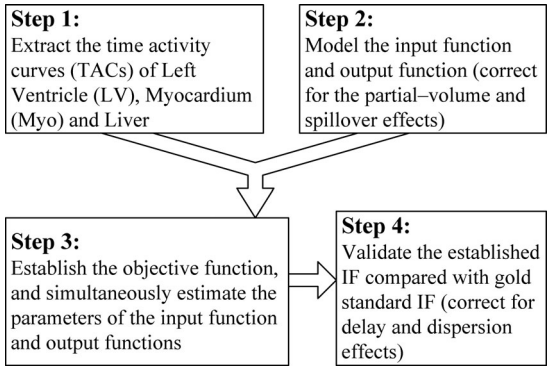

Fig. 1. Overall flowchart of the proposed method.

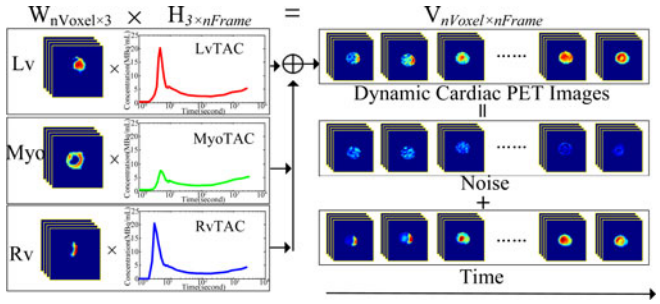

Fig. 2. Illustration of NMF decomposition on dynamic cardiac PET data.

and tissue activities. Since it has been indicated by Tantawy and Peterson that the scaled TAC of the liver at a later time can be used as an approximation of the cardiac whole-blood TAC [10], we utilized this approximated whole-blood TAC in step 3 to construct a Bayesian (*a priori*) penalty term and incorporate it into the objective function, in which three adaptive weighing factors were introduced and estimated during the optimization process in order to improve accuracy. The parameters of the IF and OFs were then estimated by fitting the Lv and Myo TACs to their corresponding compartment outputs. The delay and dispersion effects were finally taken into consideration by a two-compartment model. We tested the proposed method with 20 mouse studies to demonstrate its effectiveness.

II. Method

A. TACs Extraction of the Liver, Lv and Myo

Liver VOI was manually drawn on the summed slice since the liver could be clearly visible, and then the liver TAC was generated. However, because of the small size of Lv and Myo as well as the partial-volume and spillover effects, an accurate definition of their VOIs was difficult, which would affect the subsequent TACs extraction. We proposed a CNMF-based method to automatically extract the TACs of Lv and Myo.

1) Constraint of Nonnegative Matrix Factorization: The nonnegative matrix factorization (NMF) method was proposed by Lee and Seung in [11]. In general, NMF factorizes a nonnegative matrix into two nonnegative matrix factors $W_{n\times k}$ and $H_{k\times n}(k<n, k<m)$ while minimizing the object function $f(W,H)=\parallel V-WH \parallel^2$:

$$V = WH\ . \tag{1}$$

The multiplicative updates for NMF are given by

$$H \leftarrow H \odot \frac{W^T V}{W^T W H},\quad W \leftarrow W \odot \frac{V H^T}{W H H^T} \tag{2}$$

where $\odot$ means dot product, and $\frac{A}{B}$ means dot divide, i.e., $\left[\frac{A}{B}\right]_{ij}=\frac{A_{ij}}{B_{ij}}$.

When applying NMF to dynamic cardiac PET data $V_{n\mathrm{Voxel}\times n\mathrm{Frame}}$ (nVoxel represents the number of the voxels of each frame and nFrame represents the number of the frames), $V_{n\mathrm{Voxel}\times n\mathrm{Frame}}$, which can be regarded as dynamic cardiac PET images, and this is a linear combination of three tissue (Lv, right ventricle (Rv), and Myo, i.e., $k=3$) concentrations under the assumption that the tissue TAC is the same during the whole acquisition inside the same tissue, while different tissues behave differently. $W_{n\mathrm{Voxel}\times 3}$ can be regarded as the probability distribution map matrix of the three tissues; and $H_{3\times n\mathrm{Frame}}$ can be regarded as their corresponding tissue TACs matrix. An illustration of the decomposition is shown in Fig. 2.

Even if NMF is physically intuitive and has been used as a method capable of finding the underlying part-based structure of the complex data, the solution of NMF is not unique, and not necessarily localized [12]. Thus, more constraints are needed to confine the factorization solution.

Two constraints were applied as follows.

1) *Orthogonality Constraint:* Different tissue maps (W) should be orthogonal, so as to minimize redundancy between different tissue maps (i.e., different tissues should not be overlapped)
$$W^T W = I\ .$$
2) *Scale Constraint:* The sum of the probability of a given voxel belonging to different tissues should be equal to 1, so as to rescale W and H to a proper scale
$$\sum_{j=1}^{k} W_{ij} = 1\ , \text{for all rows } i\ .$$

For the first constraint, the multiplicative updates can be given by [12]:

$$H \leftarrow H \odot \frac{W^T V}{W^T W H},\quad W \leftarrow W \odot \frac{V H^T}{W H V^T W}\ . \tag{3}$$

For the second constraint, suppose $\alpha=[\alpha_1,\alpha_2,\alpha_3]^T$, and

$$W_i = W_i \odot \alpha,\ \text{for all rows } i$$
$$H_l = \frac{H_l}{\alpha^T},\ \text{for all columns } l$$

then, we have the solution

$$\alpha = \left(\sum_{i=1}^{n\mathrm{Voxel}} W_i\right)(W^T W)^{-1}\ . \tag{4}$$

2) Subalgorithm Flowchart: The proposed methodology to extracted TACs of Lv and Myo is shown in Fig. 3. A detailed description of the steps is given as follows.

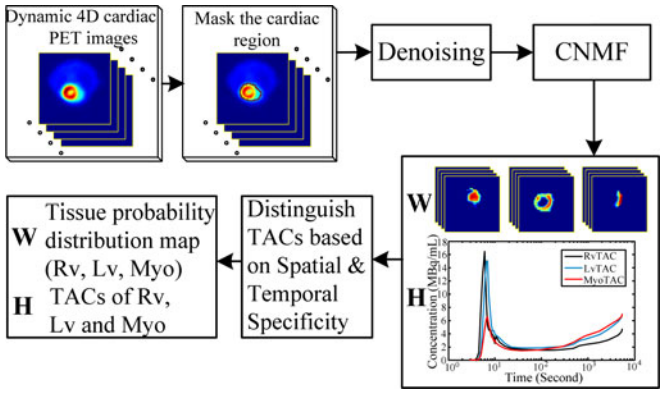

Fig. 3. Flowchart of automatically extracting TACs of Rv, Lv and Myo.

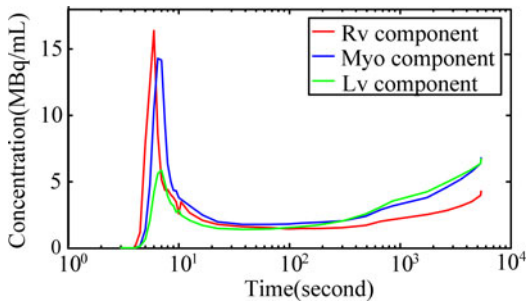

Fig. 4. Spatial and temporal specificity profiles of tissue TACs.

1) *Masking of the Mouse Cardiac Region:* The mouse heart was segmented based on Otsu [13] to exclude the background and tissues with lower activity. With this masking, only three cardiac tissue components (Lv, Rv, and Myo) were separated. After masking, the masked dynamic cardiac PET images were reorganized into its vector form $X_{n\mathrm{Voxel}\times n\mathrm{Frame}}$.
2) Smoothing and denoising: $X_{n\mathrm{Voxel}\times n\mathrm{Frame}}$ was then smoothed and denoised by means of the discrete cosine transform [14], and was denoted by $V_{n\mathrm{Voxel}\times n\mathrm{Frame}}$.
3) Separation of cardiac tissue components: Then, CNMF was applied to decompose $V_{n\mathrm{Voxel}\times n\mathrm{Frame}}$ into two matrices: three tissue probability distribution map matrices $(W_{n\mathrm{Voxel}\times 3})$ and their corresponding TACs matrix $(H_{3\times n\mathrm{Frame}})$.
4) Distinction of each tissue component: After the decomposition, since the CNMF decomposition order was unfixed, we utilized the spatial and temporal specificity of the tissue TACs to distinguish each tissue component. The tissue TACs' spatial and temporal specificity means that the ^{18} F-FDG concentration reaches the peak value first in Rv, then in Lv, and at last accumulates in Myo, as shown in Fig. 4; see [15] for more details. Then, the TACs of Lv $(\mathrm{PET}_{\mathrm{Lv}})$ and Myo $(\mathrm{PET}_{\mathrm{Myo}})$ were obtained from $H_{3\times n\mathrm{Frame}}$.

B. Modeling the IF and OFs

We used the well-established two-tissue compartment model here to describe the rates of changes in concentration in the mouse heart

$$\begin{cases} \dfrac{d}{dt}C_e(t) = K_1 C_{p\_\mathrm{Lv}}(t) - (k_2+k_3)C_e(t) + k_4 C_m(t) \\ \dfrac{d}{dt}C_m(t) = k_3 C_e(t) - k_4 C_m(t) \end{cases} \tag{5}$$

where $C_{p\_\mathrm{Lv}}(t), C_e(t)$, and $C_m(t)$ are the ideal ^{18}F-FDG plasma TAC in Lv, the ^{18}F-FDG concentration and the phosphorylated ^{18}F-FDG (^{18}F-FDG-6P) concentration in Myo tissue, respectively. K_1, k_2, k_3, and k_4 are the transfer rate constants between compartments. The metabolic rate of glucose can be calculated by

$$\mathrm{MRGlu} = \frac{C_{\mathrm{glu}}}{\mathrm{LC}} \cdot K_i = \frac{C_{\mathrm{glu}}}{\mathrm{LC}} \cdot \frac{K_1 k_3}{k_2 + k_3} \tag{6}$$

where C_{glu} is the glucose concentration in blood, LC is the lumped constant, and K_i is the ^{18}F-FDG influx constant.

Because of the partial-volume and spillover effects, the measured TACs of Lv $(\mathrm{PET}_{\mathrm{Lv}})$ and Myo $(\mathrm{PET}_{\mathrm{Myo}})$ were modeled as a linear combination of tissue activities, i.e., the Myo uptake $(C_e(t) + C_m(t))$ and the ideal TAC in Lv $(C_{a\_\mathrm{Lv}}(t))$:

$$\begin{cases} m_{\mathrm{Lv}} = C_{a\_\mathrm{Lv}}(t) + a \times (C_e(t) + C_m(t)) \\ m_{\mathrm{Myo}} = b \times C_{a\_\mathrm{Lv}}(t) + (C_e(t) + C_m(t)) \end{cases} \tag{7}$$

where m_{Lv} and m_{Myo} are the model-predicted outputs of TACs of Lv and Myo, respectively. The mixing coefficients a and b are within the range [0 1]. $C_{a\_\mathrm{Lv}}(t)$ is the ^{18}F-FDG whole-blood TAC in Lv, and can be modeled as [15]:

$$C_{a\_\mathrm{Lv}}(t) = \begin{cases} 0, \text{ if } t < \tau \\ [A_1(t-\tau) - A_2 - A_3]\, e^{\lambda_1(t-\tau)} + A_2 e^{\lambda_2(t-\tau)} \\ + A_3 e^{\lambda_3(t-\tau)}, \text{ otherwise.} \end{cases} \tag{8}$$

The IF that indicates the ^{18}F-FDG plasma TAC in Lv, i.e., $C_{p\_\mathrm{Lv}}(t)$ can be calculated by [16] :

$$C_{p\_\mathrm{Lv}}(t) = C_{a\_\mathrm{Lv}}(t) \times R_{\mathrm{PB}} \tag{9}$$

where R_{PB} is the ratio of the plasma to the whole-blood TAC as a function of blood-sampling time (in minutes) after tracer injection, and $R_{\mathrm{PB}} = 0.386e^{-0.191t} + 1.165$.

C. Simultaneous Estimation

1) Objective Function: The parameters of the IF and OFs can be estimated by fitting the Lv and Myo TACs to their corresponding compartment outputs, that is to solve the minus value of the objective function as

$$O(\mathbf{p}) = \sum_{i=1}^{n\mathrm{Frame}} [(m_{\mathrm{Lv},i} - \mathrm{PET}_{\mathrm{Lv},i})^2 + (m_{\mathrm{Myo},i} - \mathrm{PET}_{\mathrm{Myo},i})^2]. \tag{10}$$

However, since this objective function is insufficient to obtain accurate parameter values, traditionally two2 or three 3 extra blood samples at a later time were incorporated into the objective function to ensure the estimation accuracy. However, it is still invasive. To overcome this drawback, we utilized the liver TAC to construct the Bayesian (*a priori*) penalty term to

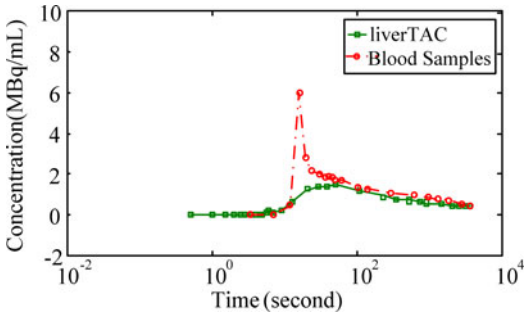

Fig. 5. Relationship between the arterial blood samples and liver TAC.

TABLE I
MEAN AND SD OF THE RATIOS

	1 *min*	10 *min*	20 *min*	30 *min*	40 *min*
$Mean_\theta$	1.2653	1.5257	1.4782	1.1304	0.8749
SD_θ	0.1475	0.2550	0.2909	0.2491	0.3847

be incorporated into the objective function, since it has been reported that the liver has relatively low ^{18}F-FDG retention because it is highly vascularized and the liver TAC at a later time can be used as an approximation of the whole-blood TAC [10]. Fig. 5 illustrates the relationship between the arterial blood samples and the liver TAC, which shows that the liver TAC has an exponentially decaying part similar to that of whole-blood TAC.

Based on the relations between the arterial blood samples and the liver TAC, we define a random variable θ:

$$\theta_j = C_a(t_j)/\mathrm{PET}_{\mathrm{liver}}, j = 1, 2, \ldots, m\ . \tag{11}$$

Here, θ can be assumed to be subordinate to the normal distribution according to the Bayesian probability theory. The mean and the standard deviation (SD) of θ were calculated using five randomly chosen studies (m10438, m10660, m17437, m17464, and m17822) as the training datasets at five time points (see Table I) in this study.

The Bayesian penalty term can be given by [17]:

$$\mathrm{Bay}(C_{a\_\mathrm{Lv}}) = \sum_{j=1}^{m} \left[\frac{C_{a\_\mathrm{Lv}}(t_j) - \mathrm{PET}_{\mathrm{liver},j} \times \mathrm{Mean}_{\theta_j}}{\mathrm{PET}_{\mathrm{liver},j} \times \mathrm{SD}_{\theta_j}} \right]^2 . \tag{12}$$

The reason it uses ratios in multiple time points but not a unified ratio to construct the Bayesian penalty term is: the tested mice datasets from MQP database were collected over a period of several years. Due to changes in the experimental environment, large differences existed among individuals, which made a unified ratio less accurate.

Incorporating the Bayesian penalty term into the objective function, the objective function can be expressed as

$$O(\mathbf{p}) = \omega_1 \sum_{i=1}^{n\mathrm{Frame}} \left(\mathrm{m}_{\mathrm{Lv},i} - \mathrm{PET}_{\mathrm{Lv},i}\right)^2 + \omega_2 \sum_{i=1}^{n\mathrm{Frame}} \left(\mathrm{m}_{\mathrm{Myo},i} - \mathrm{PET}_{\mathrm{Myo},i}\right) + \omega_3\ \mathrm{Bay}(C_{a\_\mathrm{Lv}}) \tag{13}$$

TABLE II
INITIAL VALUES AND BOUNDS FOR ALL PARAMETERS TO BE ESTIMATED

Parameters	A_1 (MBq/min/mL)	A_2 (MBq/mL)	A_3 (MBq/mL)	λ_1 (min^{-1})	λ_2 (min^{-1})	λ_3 (min^{-1})	τ (min^{-1})	K_1 (min^{-1})
Initial value	5703.27	4.9953	2.7580	-144.2	-13.62	-0.034	0.080	0.5
upper bound	20000	20	5	0	0	0	3	1
lower bound	1000	0	0	-300	-20	-0.1	0.150	0.001
Parameters	k_2 (min^{-1})	k_3 (min^{-1})	k_4 (min^{-1})	a	b	ω_1	ω_2	ω_3
Initial value	0.5	0.5	0.001	0.1	0.1	1.68	1.33	0.66
upper bound	2	1	0.001	1	1	10	10	1
lower bound	0.001	0.0001	0.0001	0	0	0.1	0.1	0.001

where ω_1, ω_2, and $\omega_3$indicate the self-adaptive weighing factors corresponding to the three terms of the objective function. The values of the weighing factors are also estimated during the optimization process by the nonlinear least-squares method. Thus, the parameters to be estimated are noted as $\mathbf{p} = [\tau, A_1, A_2, A_3, \lambda_1, \lambda_2, \lambda_3, K_1, k_2, k_3, k_4, a, b, \omega_1, \omega_2, \omega_3]$.

2) Initialization: The initial value and bound for $\mathbf{p}$ influence the iterative speed and computation complexity; therefore, it is important to choose suitable initial values.

For each dataset, the initial values of the parameters of IF, i.e., $A_1, A_2, A_3, \lambda_1, \lambda_2, \lambda_3, \tau$, were acquired by fitting an approximate curve of $C_{a\_\mathrm{Lv}}(t)$ ($C_{a\_\mathrm{Lv\_approx}}(t)$) to the whole-blood TAC model. First, $C_{a\_\mathrm{Lv\_approx}}(t)$ was constructed with the image-derived Lv TAC ($\mathrm{PET}_{\mathrm{Lv}}$) and the average values of the real arterial blood samples of the training datasets. The early time (the first 30 s) points of the approximate curve were obtained by the interpolation of $\mathrm{PET}_{\mathrm{Lv}}$, while the later part was acquired by averaging the interpolated real arterial blood samples of five randomly chosen training datasets at a later time (after 60 s). Then, we utilized the $C_{a\_\mathrm{Lv\_approx}}(t)$ to fit the parameters of the whole-blood TAC model, described in (8), to obtain the initial values of the parameters, i.e., $A_1, A_2, A_3, \lambda_1, \lambda_2, \lambda_3, \tau$ which could help to reduce computational complexity and avoid falling into the local minimum during optimization. Taking m17919 for example, the initial values of $A_1, A_2, A_3, \lambda_1, \lambda_2, \lambda_3, \tau$, were 5703.27 MBq/min/mL, 4.9953 MBq/mL, 2.7580 MBq/mL, -144.2 min^{-1}, -13.62 min^{-1}, -0.034 min^{-1}, 0.080 min respectively. We did not give the general initial values of these parameters in Table II, for they vary with datasets.

Initial values for parameters K_1, k_2, k_3, k_4, a, b, listed in Table II, were manually set according to the estimated results in [9], and used for all the tested microPET images in our study.

Additionally, in order to acquire the initial values of the self-adaptive weighing factors $(\omega_1, \omega_2, \omega_3)$, we performed many trials for each of the aforementioned five chosen training datasets with a series of different initial values. For each of the training dataset, we set a series of different weighting values as the initial values of $(\omega_1, \omega_2, \omega_3)$, and completed the optimization of the objective function [described in (13)]. The values of $(\omega_1, \omega_2, \omega_3)$, that minimized the value of the objective function were the proper values for this dataset. Then,

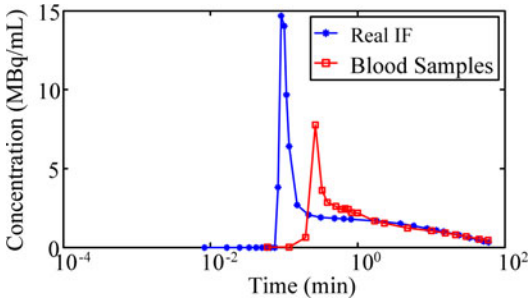

Fig. 6. Real IF in Lv and the blood samples during the whole scan.

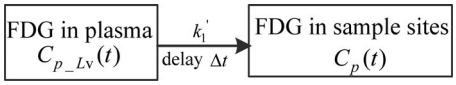

Fig. 7. Two-compartment model to describe the delay and dispersion effects.

we used the average of the five corresponding proper values for $(\omega_1, \omega_2, \omega_3)$ as the initial values for the weighing factors. The initial values of weighing factors listed in Table II were used for all the tested microPET images in our study.

3) Optimization: The Compartment Model Kinetic Analysis Tool (COMKAT) [18], [19] was used to solve the models and estimate parameters.

D. Input Function Validation

Following the optimization process after the parameters $A_1, A_2, A_3, \lambda_1, \lambda_2, \lambda_3, \tau$ were obtained, the IF can be calculated from (9).

When comparing the estimated IF (EIF) with the gold standard blood samples, the delay and dispersion effects should be considered. Because the blood samples were drawn from the right femoral artery and not directly from the Lv cavity, there was a time interval between the peak of Lv and the femoral artery, as shown in Fig. 6. We constructed a two-compartment model to describe these effects (shown in Fig. 7)

$$\frac{dC_p(t)}{dt} = k_1' C_{p\_\mathrm{Lv}}(t - \Delta t) - k_1' C_p(t) \tag{14}$$

where k_1' is the dispersion rate constant and Δt indicates the time delay. Five datasets with the most abundant early-time ($<$1 min) blood sample data were used as training sets to calculate mean values of both k_1' and Δt. Then, these mean values were applied for all datasets. Finally, the delayed and dispersed EIF (DDEIF) is compared with the gold standard IF.

III. Experimental Results

A. Data Acquisition

The tested microPET images were downloaded from the Mouse Quantitation Program (MQP) database [20] (http://dragon.nuc.ucla.edu/mqp/index.html), as provided by UCLA. These microPET images were obtained by about a 60-min PET scan (microPET Focus 220; Siemens Medical Solutions USA, Inc.,) immediately after the injection of ^{18}F-FDG (tail vein bolus) into the mouse. The typical frame rates were: $16 * 0.5$ s, $1 * 2$ s, $1 * 4$ s, $1 * 6$ s, $1 * 15$ s, $3 * 30$ s, $1 * 60$ s, $1 * 2$ min, $3 * 3$ min, and $5 * 15$ min, and each frame of the image data was reconstructed by FBP with $128 * 128 * 95$ voxels. Several blood samples (5–22) were taken from a femoral catheter to obtain the wholeblood TACs. Blood-to-plasma conversion was performed as described in (9). Twenty fasted or nonfasted C57/BL6 mice datasets randomly chosen from the database were used to verify our method.

B. Evaluation Criteria

The extracted TACs of Lv and Myo were validated by calculating the area under curves error

(AUCE) and the root mean square error (RMSE), and comparing them with TACs extracted from manually drawn ROIs as the standard reference.

To evaluate the performance of our proposed estimation method, both the direct and indirect comparisons between DDEIF and gold standard blood samples were conducted in terms of visual comparison, such as the AUCE and the ^{18}F-FDG influx constant K_i. Three kinds of influx constants K_i solved by two different widely used methods were compared, that is, $K_{i,\mathrm{DDEIF}}$ and $K_{i,\mathrm{GS}}$ were calculated with the gold standard IF and DDEIF by the Patlak method, and $K_{i,\mathrm{Model}}$ was computed by the model-based method ($K_{i,\mathrm{Model}} = \frac{K_1 k_3}{k_2 + k_3}$). The Patlak method is preferred to be used for its efficiency in computation and easy implementation; while the model-based method is well known for the fact that it can estimate all of the transfer rate constants. By comparing the $K_{i,\mathrm{DDEIF}}$ and $K_{i,\mathrm{GS}}$, we could validate the accuracy of EIF directly, while by comparing the $K_{i,\mathrm{Model}}$ to $K_{i,\mathrm{GS}}$, we could validate the accuracy of individual transfer rate constants (K_1, k_2, k_3, k_4), and prove the correctness of the estimated IF indirectly. By both comparisons, we could verify our proposed estimation method more comprehensively.

C. Results

1) Extraction of Lv and Myo TACs: The extraction of probability distribution maps (Lv, Rv, and Myo) and their TACs with our proposed CNMF method was satisfactory in all of the 20 normal mouse studies. Fig. 8 shows the segmentation results (the probability distribution maps, PDM) and corresponding TACs extracted using the traditional NMF method and the CNMF method in one sample study (m10610). It can be observed that the CNMF method provided more localized, part-based probability distribution maps and more reasonable TACs than the traditional NMF.

In order to get insight into the robustness of our proposed CNMF method, both qualitative and quantitative comparisons of TACs were performed. Fig. 9 demonstrates the differences of TACs extracted by the traditional NMF method, our CNMF method, and the standard reference. It can be noted that the TACs of our proposed CNMF method were much closer to the standard references than the traditional NMF method, especially for those of the Lv and Myo. Quantitative comparisons of the AUCE and RRMSE between the traditional NMF method, our CNMF method, and the standard reference with 20 datasets are

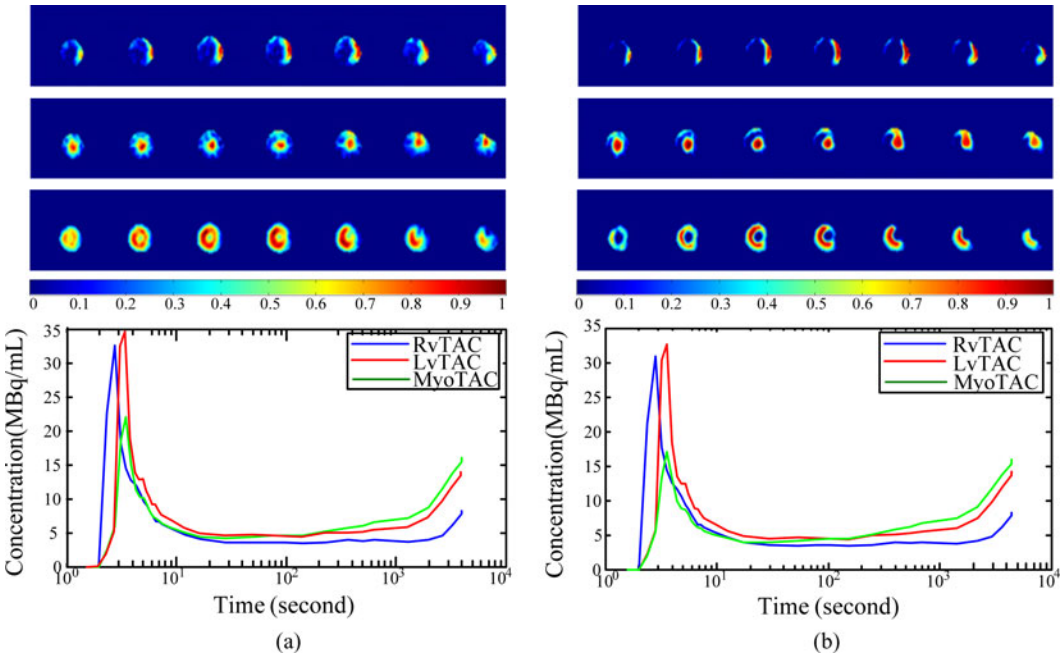

Fig. 8. Comparison of probability distribution maps and TACs extracted with NMF and CNMF methods for the dataset m10610. The first three rows separately demonstrate the segmentation results (PDM) of the Rv, Lv, and Myo, followed by their TACs at different times. (a) NMF. (b) CNMF.

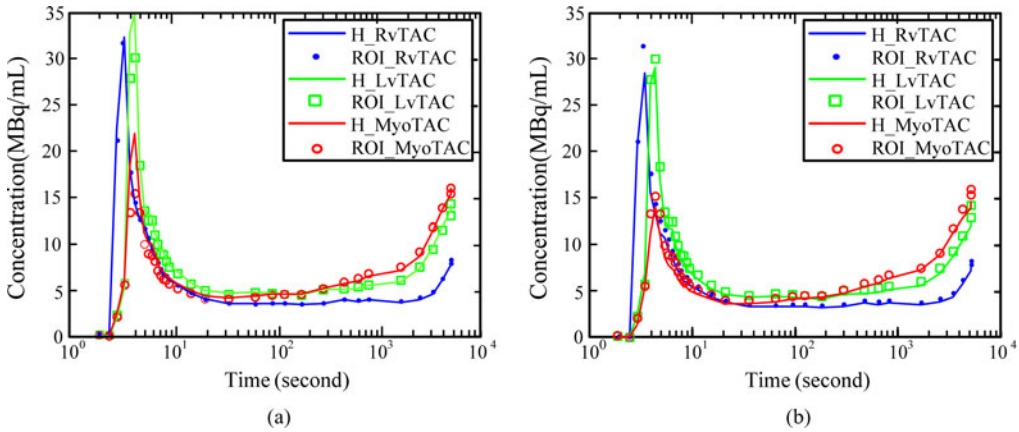

Fig. 9. Visual comparison of TACs extracted by NMF and CNMF (indicated by H_RvTAC, LvTAC, H_MyoTAC) with the standard reference (indicated by ROI_RvTAC, ROI_LvTAC, ROI_MyoTAC), respectively. (a) NMF. (b) CNMF.

TABLE III
MEAN AND STANDARD DEVIATION OF AUCE AND RMSE OF TACS FOR 20 DATASETS EXTRACTED BY NMF AND CNMF COMPARED WITH THE STANDARD REFERENCE

	LvTAC	**MyoTAC**	**RvTAC**
AUCE (NMF)	0.1197±0.0995	0.0479±0.0597	0.1048± 0.0788
AUCE (CNMF)	**0.0281±0.0180**	**0.0345±0.0214**	**0.0301±0.0174**
RMSE(NMF)	0.3008±0.2312	0.1397±0.0688	0.1009±0.0581
RMSE(CNMF)	**0.0310±0.0179**	**0.0422±0.0206**	**0.0339±0.0153**

shown in TABLE III. We can see that our proposed CNMF method produced an obviously smaller AUCE (2.8–3.5%) and RRMSE (3.1–4.3%) for both Lv and Rv TACs than the NMF method (4.8–12.0%, 10.1–30.1%, respectively), while for the Myo TAC, the proposed CNMF method did not have many differences with the NMF method on the AUCE, but generated a smaller RRMSE.

2) Validation of the Input Function: To compare our EIF with the gold standard blood samples, the dispersion and delay were considered. In this study, the five random datasets used to calculate the average values of the dispersion factor k_1' and the delay Δt using the delay and dispersion correction model were m17385, m17437, m17464, m17709 and m17822. The estimated mean values of k_1' and Δt were 84.034 and 0.079 min, respectively.

Fig. 10 compares the plots of DDEIF and the gold standard blood samples with two sample datasets (1 unfasted+1 fasted). Taken the delay and dispersion into account, the estimated IF shows a good coincidence between the blood samples and DDEIF. The width of the peak was very similar and the tail

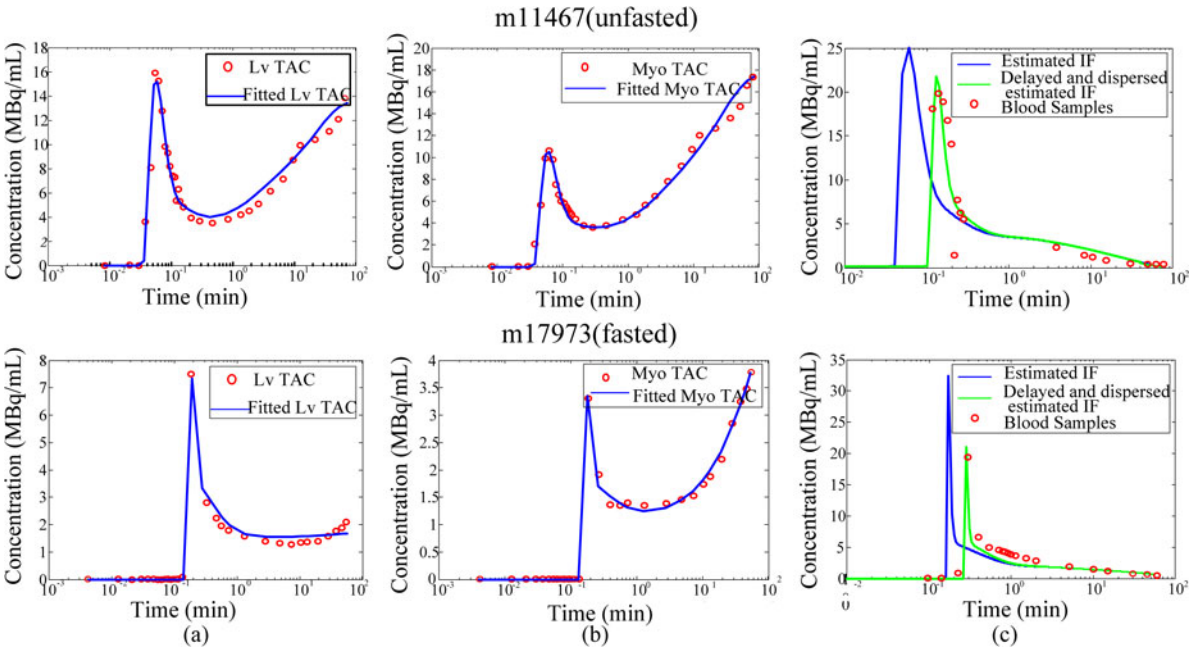

Fig. 10. Estimation plots of the estimated IF for two sample studies (1 unfasted study + 1 fasted study). (a) and (b) are image-extracted Lv/Myo TACs and model-fitted Lv/Myo TACs. (c) Comparison of the EIF (the ideal TAC in Lv cavity), the DDEIF and gold standard blood samples.

of the DDEIF coincided well. Fig. 12(a) plots the correlation between the areas under curves (AUCs) of gold standard IFs and DDEIFs, with a correlation coefficient of 0.969, and the average value of AUCE was 7.237% $\pm$ 6.742%.

Table IV shows parameters estimated for all 20 datasets as well as three kinds ofK_i. It is noted that the average K_i error between $K_{i,\mathrm{DDEIF}}$ and $K_{i,\mathrm{GS}}$ was 4.910% $\pm$ 9.810%, and 10.621% $\pm$ 13.121% between $K_{i,\mathrm{Model}}$ and $K_{i,\mathrm{GS}}$. The correlation coefficients were 0.992 and 0.970, respectively (see Fig. 11 (b) and (c) shows this correlation.) The results of the t-test yielded a $p > 0.05$, indicating that the differences in the K_i estimates did not reach a level of statistical significance. All of these results proved the correctness and effectiveness of the proposed method.

IV. Discussion

In this paper, we proposed a noninvasive estimation method of the IF in dynamic mouse ^{18}F-FDG microPET studies. Comparing with the traditional simultaneous estimations in [1] and [9], the innovation of our method could be summarized as follows: 1) the incorporation of the orthogonality and scale constraint in NMF to extract LvTAC and MyoTAC automatically and accurately; 2) the construction of the Bayesian (*a priori*) term based on the strong correlation between the liver TAC and the whole-blood TAC at a later time during optimization; 3) the introduction of three self-adaptive weighing factors for optimization; 4) the correction of the partial-volume, spillover, delay and dispersion effects to perform an accurate comparison between EIF and the gold standard IF. Owing to the aforementioned innovations, we estimated the IF noninvasively and accurately, which could be helpful in the clinical application of dynamic PET.

The accurate extraction of the tissue TACs is the precondition of the following fitting process and it affects the estimation results. In order to analyze the issue clearly, we performed some additional experiments by fitting the less accurate TACs, which were constructed by multiplying the accurate TACs extracted from manually drawn ROIs (standard references) by a series of error factors (1.05, 1.1, and 1.2), to the objective function and then acquired the kinetic parameters and DDEIF. When the errors of TACs were small (the error factor was 1.05), the average error between $K_{i,\mathrm{DDEIF}}$ and $K_{i,\mathrm{GS}}$ was 7.073% $\pm$ 5.844%, and 11.4 $\pm$ 21.8% between $K_{i,\mathrm{Model}}$ and $K_{i,\mathrm{GS}}$. The errors are relatively small, which means that small errors of TACs do not have significant effect on the estimated parameters. However, when the errors of TACs were larger, e.g., the error factors were 1.1 and 1.2, the average errors between $K_{i,\mathrm{DDEIF}}$ and $K_{i,\mathrm{GS}}$ were 11.3% $\pm$ 8.69% and 18.0% $\pm$ 16.4%, and the average errors between $K_{i,\mathrm{Model}}$ and $K_{i,\mathrm{GS}}$ were 12.6 $\pm$ 12.0% and 24.2 $\pm$ 23.0%. This means the large error of TACs affects the accuracy of the estimated parameters to a large extent. Therefore, the accuracy of the tissue TACs is very important in the estimation process.

Considering that the manual definition of the ROIs is subjective and requires a lot of clinical experience, an automatic segmentation and extraction method are quite necessary. Many matrix decomposition-based methods have been proposed in the segmentation of images, such as the Principal Component Analysis (PCA) [21] and ICA [22]. However, these methods allow negative entries in the matrix factors W and H, even if the elements of the initial input matrix element are positive. This makes the combination of eigenvectors possibly be involved in a complex cancellation between positive and negative numbers, which means that many individual eigenvectors lack intuitive meaning. On the contrary, NMF makes the nonzero elements of

TABLE IV
ESTIMATED PARAMETERS AND STANDARD DEVIATION FOR ALL MOUSE STUDIES

Study	K_1	k_2	k_3	k_4	τ	A_1	A_2	A_3	λ_1	λ_2	λ_3	$K_{i,GS}$	$K_{i,EIF}$	$K_{i,Model}$
m09940	0.2141	0.5172	0.2322	6.94e-05	0.1090	2574.7	0.9430	0.8763	-102.82	-4.288	-0.0384	0.0650	0.0658	0.0663
m10438	0.1361	4.19e-04	0.1832	1.58e-10	0.1299	8366.5	6.3721	3.4118	-107.36	-4.419	-0.0294	0.0856	0.0866	0.1358
m10550	0.2017	0.0242	0.4831	2.86e-14	0.0632	4814.1	3.2020	2.4255	-88.758	-1.223	-0.0445	0.2120	0.1989	0.1921
m10660	0.1361	2.67e-14	0.1170	8.97e-3	0.0925	3171.6	2.0729	1.3126	-94.998	-0.754	-0.0331	0.1304	0.1281	0.1361
m10861	0.1105	1.55e-05	0.2799	3.91e-4	0.0449	13841	7.3510	2.4045	-168.97	-7.114	-0.0239	0.1208	0.1206	0.1105
m10911	0.2256	0.0190	0.3489	1.50e-10	0.0628	9799.2	5.0554	2.0709	-117.2	-1.478	-0.0292	0.2318	0.2301	0.2139
m10948	1.0028	0.7020	0.1405	2.26e-14	0.0551	7770.4	10.338	1.6998	-113.54	-7.868	-0.0154	0.2029	0.2096	0.1673
m11043	0.3495	0.5044	0.3182	7.84e-5	0.0951	7941.2	10.992	1.6940	-115.68	-8.601	-0.0200	0.1244	0.1246	0.1352
m11082	0.2922	0.4953	0.3756	4.07e-10	0.0448	5201.6	2.7937	2.0144	-65.119	-0.823	-0.0482	0.1340	0.1475	0.1260
m11122	0.1223	0.0249	0.4214	3.85e-6	0.0202	2997.9	10.522	2.1315	-108.04	-16.835	-0.0486	0.1421	0.1292	0.1155
m17437	0.0970	0.2907	0.1464	1.48e-4	0.0514	3093.8	6.1833	1.3249	-154.69	-14.845	-0.0087	0.0275	0.0287	0.0325
m17709	0.3080	0.4282	0.2740	4.84e-5	0.0365	10952	8.0705	3.6975	-150.45	-8.556	-0.0289	0.1185	0.1197	0.1202
m17822	0.4386	0.7157	0.2327	1.48e-4	0.0765	9392.0	5.8564	3.2208	-111.61	-5.234	-0.0259	0.1333	0.1155	0.1084
m17919	0.2442	0.6170	0.1159	2.23e-3	0.0864	6112.6	3.0841	1.0949	-187.48	-12.971	-0.0206	0.0386	0.0394	0.0386
m17973	0.2572	0.9370	0.2535	7.78e-14	0.1633	8028.7	2.5850	1.3787	-160.62	-3.124	-0.0167	0.0534	0.0524	0.0547
m18482	0.1185	0.4547	0.3298	6.35e-03	0.1106	7458.8	5.8744	2.2416	-186.35	-10.268	-0.0145	0.0418	0.0420	0.0498
m11467	0.6804	0.3062	0.1949	3.00e-05	0.0431	2984.8	10.305	2.3365	-114.73	-13.487	-0.0417	0.2561	0.2584	0.2617
m17332	0.0829	7.54e-06	0.1128	8.11e-3	0.0256	4013.2	2.2665	1.4189	-179.38	-14.058	-0.0320	0.0873	0.0862	0.0829
m17884	0.1732	0.6546	0.0757	2.06e-4	0.0555	2397.1	2.4751	2.0921	-60.161	-1.502	-0.0156	0.0182	0.0233	0.0179
m18778	0.1639	0.6305	0.1842	1.46e-8	0.1414	3263.0	0.3607	2.7304	-73.025	-9.797	-0.0188	0.0363	0.0361	0.0370
K_i Error	-	-	-	-	-	-	-	-	-	-	-	-	4.910±9.810	10.62±13.12
Corr. Coef	-	-	-	-	-	-	-	-	-	-	-	-	0.9917	0.9701
t test P value	-	-	-	-	-	-	-	-	-	-	-	-	0.5851	0.4834

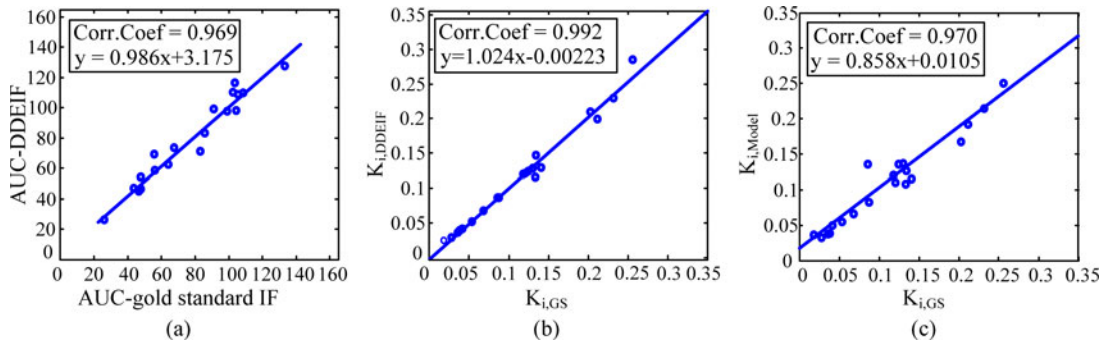

Fig. 11. (a) Correlation plot of the AUCs of gold standard IFs versus the DDEIFs ($r = 0.969$, with AUCE $= 7.237\% \pm 6.742\%$). (b) Correlation plot of $K_{i,\mathrm{DDEIF}}$ versus $K_{i,\mathrm{GS}}$($r = 0.992$, with the average error as $4.910\% \pm 9.810\%$). (c) Correlation plot of $K_{i,\mathrm{Model}}$ versus $K_{i,\mathrm{GS}}$ ($r = 0.970$, with the average error as $10.621\% \pm 13.121\%$).

W and H all positive with the connectivity constraints, which leads to the parts-based eigenvectors with intuitive meaning, for only additive combinations are allowed. Thus, only NMF-based methods were used and compared in the extraction of the tissue TACs. Based on the traditional NMF method, we added both an orthogonality constraint and scale constraint to improve the extraction of TACs in accuracy, which can be seen clearly in Fig. 9 and Table III, especially for the Lv and Rv. For the AUCE of the Myo, the two methods seem to have few differences, whereas from the RRMSE and Fig. 9, it is confirmed that our method generated better segmentation results and thus had more accurate TACs for Myo. The accuracy and robustness of the proposed method could also be observed from the CNMF method which gives localized and part-based probability distribution maps and reasonable TACs in Table III. From Table III, we can see that CNMF provides TACs automatically with sufficiently small errors to accomplish the fitting process without affecting the accuracy of the estimated parameters.

In order to simulate the actual process *in vivo* and apply the kinetic model accurately, we modeled the TACs of Lv and Myo by taking the partial-volume and spillover effects between the two tissues into consideration. The reason why we did not take

the effect of Rv into consideration was that we did not get better results when the effects of Rv were added into the modeling, possibly due to the introduction of more free variables. Besides, it increased the complexity and reduced the efficiency during the estimation.

In our experience, the impact of TACs was less than IF, for the introduction of mixing coefficients a and b partially eliminated the effects brought on by the inaccuracy of TACs. The inaccuracy of IF, especially the tail of IF, affected the estimation of the kinetic parameters to a large extent. In our previous work about the simultaneous estimation, at least 1 later blood sample was required in the fitting process to improve accuracy [23]. In this study, a Bayesian term utilizing the ratios (θ) of the whole-blood TAC and the liver TAC was constructed instead to calibrate the EIF. In order to fulfill the completely noninvasive estimation of the input function, we took the average value and variance of the ratios θ at multiple time points from five randomly chosen studies as *a priori* knowledge to construct the Bayesian term. After a large number of trials, the use of the five time points [1, 10, 20, 30, and 40 min] produced the most accurate estimation of the whole-blood TAC. The inclusion of an additional time point did not improve accuracy, but the removal of any time point would reduce accuracy.

Furthermore, during the estimation, the choice of ω_1, ω_2, and ω_3 became very important for the estimation. The larger ω_1 and ω_2 are, the more accurate the EIF curve is at early time points, while the larger ω_3 is, the more accurate the EIF curve is at a later time. Therefore, a compromise must be made to get the best results for the EIF in both the early time and the later time. For this purpose, we set the adaptive weighing factors during the estimation. The AUC of the DDEIF and $K_{i,\mathrm{EIF}}$ are not only highly correlated (correlation coefficients close to 1) to, but also highly comparable (regression slopes close to 1 and intercepts close to 0) with the AUC of the gold standard IF and $K_{i,\mathrm{GS}}$, which can be seen in Figs. 10 and 11. Table IV shows that the $K_{\mathrm{i,GS}}$ and $K_{i,\mathrm{DDEIF}}$, as well as the$K_{i,\mathrm{GS}}$ and $K_{i,\mathrm{Model}}$, did not statistically detect the exception according to the results of the *t*-test. All of these show that the DDEIF has a good coincidence with the gold standard blood samples. Note that Table IV shows that the error between $K_{i,\mathrm{Model}}$ and $K_{i,\mathrm{GS}}$ was approximately 10.62%, which was much larger than that between $K_{i,\mathrm{DDEIF}}$ and $K_{i,\mathrm{GS}}$. This is partly due to the assumption of $k_4 = 0$ when calculating $K_{i,\mathrm{GS}}$ and $K_{i,\mathrm{DDEIF}}$ using the Patlak method. In contrast, the nonlinear least-squares method was used for the simultaneous estimation on condition of $k_4 \neq 0$, which can be seen in column k_4 in Table IV. Additionally, in some studies, the blood samples were so few that solving $K_{i,\mathrm{GS}}$ and $K_{i,\mathrm{DDEIF}}$ using the Patlak method would generate errors. This may be another reason for the large errors between $K_{i,\mathrm{DDEIF}}$ and $K_{i,\mathrm{GS}}$, and probably $K_{i,\mathrm{Model}}$ and $K_{i,\mathrm{GS}}$.

For the quantitative analysis of dynamic PET images, the ^{18}F-FDG PTAC that measured by frequent blood sampling, is generally required as the input function for the tracer kinetic modeling technique. This invasive feature greatly limits its clinical application. Our study provides an alternative noninvasive method to quantify the metabolic rate of glucose and other meaningful physiological parameters for dynamic ^{18}F-FDG PET studies. The calculation of the physiological parameters, especially the metabolic rate of glucose, could aid the diagnosis of the malignancy, myocardial infarction, and are important for the development of new drug research and development. This could accelerate the clinical application for the dynamic PET.

V. Conclusion

In this paper, we first proposed a new CNMF-based method to automatically segment dynamic mouse cardiac ^{18}F-FDG MicroPET images (Lv, Rv, and Myo) while simultaneously extracting their TACs. The proposed CNMF method not only utilizes tissue specificity, i.e., the time-dependent behavior is the same inside the same tissue during the whole acquisition, while different tissues behave differently, but also imposes the orthogonality and scale constraints when applying the CNMF to dynamic PET images. The orthogonality constraint minimizes redundancy between different tissue maps, and the scale constraint recovers the original scale of TACs.

Based on the extracted TACs of Lv and Myo, we then proposed a novel noninvasive input function estimation method via the simultaneous estimation of kinetic model parameters in dynamic mouse ^{18}F-FDG MicroPET studies. Since it has been reported that liver TAC at a later time is strongly correlated with the input function, a Bayesian penalty formulation was constructed and incorporated into the optimization function. The proposed estimation method also takes the partial-volume, spillover, delay, and dispersion effects into consideration. Experimental results on 20 mouse datasets demonstrated the effectiveness and robustness of the proposed method.

Acknowledgment

The authors would like to thank W. Mu, Z. Chen, X. Dai who contributed equally to this studyand wrote the paper together. X. Dai defined the research theme and designed the methods. W. Mu designed, carried out the experiments and analyzed the results.

References

[1] Y. H. Fang and R. F. Muzic, Jr., "Spillover and partial-volume correction for image-derived input functions for small-animal ^{18}F-FDG PET studies," *J. Nucl. Med.*, vol. 49, pp. 606–14, Apr. 2008.

[2] K. Chen, D. Bandy, E. Reimann, S. C. Huang, M. Lawson, D. Feng, L. S. Yun, and A. Palant, "Noninvasive quantification of the cerebral metabolic rate for glucose using positron emission tomography, ^{18}F-fluoro-2-deoxyglucose, the Patlak method, and an image-derived input function," *J. Cereb. Blood F. Met.*, vol. 18, pp. 716–723, 1998.

[3] A. P. Van Der Weerd, L. J. Klein, R. Boellaard, C. A. Visser, F. C. Visser, and A. A. Lammertsma, "Image-derived input functions for determination of MRGlu in cardiac ^{18}F-FDG PET scans," *J. Nucl. Med.*, vol. 42, pp. 1622–1629, 2001.

[4] P. T. Meyer, V. Circiumaru, C. A. Cardi, D. H. Thomas, H. Bal, and P. D. Acton, "Simplified quantification of small animal [18 F]FDG PET studies using a standard arterial input function," *Eur. J. Nucl. Med.*, vol. 33, pp. 948–54, Aug. 2006.

[5] J. Kim, P. Herrero, T. Sharp, R. Laforest, D. J. Rowland, Y. C. Tai, J. S. Lewis, and M. J. Welch, "Minimally invasive method of determining blood input function from PET images in rodents," *J. Nucl. Med.*, vol. 47, pp. 330–336, Feb. 2006.

[6] K. Chen, X. Chen, R. Renaut, G. E. Alexander, D. Bandy, H. Guo, and E. M. Reiman, "Characterization of the image-derived carotid artery input function using independent component analysis for the quantitation of

[18 F] Fluorodeoxyglucose positron emission tomography images," *Phys. Med. Biol.*, vol. 52, pp. 7055–7071, Dec. 7, 2007.

[7] J. S. Lee, D. S. Lee, J. Y. Ahn, G. J. Cheon, S. K. Kim, J. S. Yeo, K. Seo, K. S. Park, J. K. Chung, and M. C. Lee, "Blind separation of cardiac components and extraction of input function from h215 o dynamic myocardial pet using independent component analysis," *J. Nucl. Med.*, vol. 42, pp. 938–943, 2001.

[8] K. H. Su, J. S. Lee, J. H. Li, Y. W. Yang, R. S. Liu, and J. C. Chen, "Partial volume correction of the MicroPET blood input function using ensemble learning independent component analysis," *Phys. Med. Biol.*, vol. 54, pp. 1823–46, Mar. 21, 2009.

[9] G. Z. Ferl, X. Zhang, H. M. Wu, and S. C. Huang, "Estimation of the ^{18}F-FDG input function in mice by use of dynamic small-animal PET and minimal blood sample data," *J. Nucl. Med.*, vol. 48, pp. 2037–2045, 2007.

[10] M. N. Tantawy and T. E. Peterson, "Simplified [18 F] FDG image-derived input function using the left ventricle, liver, and one venous blood sample," *Mol. Imag.*, vol. 9, pp. 76–86, 2010.

[11] D. D. Lee and H. S. Seung, "Learning the parts of objects by non-negative matrix factorization," *Nature*, vol. 401, pp. 788–791, Oct. 21, 1999.

[12] C. Ding, T. Li, W. Peng, and H. Park, "Orthogonal nonnegative matrix t-factorizations for clustering," in *Proc. 12th ACM SIGKDD Int. Conf. Knowl. Discovery Data Mining*, 2006, pp. 126–135.

[13] N. Otsu, "A threshold selection method from gray-level histograms," *Automatica*, vol. 11, pp. 285–296, 1975.

[14] D. Garcia, "Robust smoothing of gridded data in one and higher dimensions with missing values," *Comput. Stat. Data Anal.*, vol. 54, pp. 1167–1178, Jun. 2012.

[15] D. Feng, S. C. Huang, and X. Wang, "Models for computer simulation studies of input functions for tracer kinetic modeling with positron emission tomography," *Int. J. Biomed. Comput.*, vol. 32, pp. 95–110, Mar. 1993.

[16] H. M. Wu, D. Troung, M. C. Kreissl, M. Prins, H. R. Schelbert, M. E. Phelps, and S. C. Huang, "Mouse plasma and whole blood difference in concentration 2-[18 F] fluoro-2-deoxy-D-glucose (18 F-FDG) concentration: Implication for quantitative mouse ^{18}F-FDG PET studies," *J. Nucl. Med.*, vol. 46, p. 204, 2005.

[17] T. Callegari, A. Caumo, and C. Cobelli, "Generalization of map estimation in SAAM II: Validation against ADAPT II in a glucose model case study," *Ann. Biomed. Eng.*, vol. 30, pp. 961–8, Jul./Aug. 2002.

[18] R. F. Muzic Jr. and S. Cornelius, "COMKAT: Compartment model kinetic analysis tool," *J. Nucl. Med.*, vol. 42, pp. 636–645, 2001.

[19] Y. H. Fang, P. Asthana, C. Salinas, H. M. Huang, and R. F. Muzic, Jr., "Integrated software environment based on COMKAT for analyzing tracer pharmacokinetics with molecular imaging," *J. Nucl. Med.*, vol. 51, pp. 77–84, Jan. 2010.

[20] S. C. Huang, H. M. Wu, D. Truong, X. Zhang, M. Prins, D. B. Stout, A. F. Chatziioannou, and H. R. Schelbert, "A public domain dynamic mouse FDG MicroPET image data set for evaluation and validation of input function derivation methods," in *Proc. IEEE Nucl. Sci. Conf. Rec.*, 2006, pp. 2681–2683.

[21] M. Lopez, J. Ramirez, J. M. Gorriz, D. Salas-Gonzalez, I. Alvarez, F. Segovia, and C. G. Puntonet, "Automatic tool for Alzheimer's disease diagnosis using PCA and Bayesian classification rules," *Electron. Lett.*, vol. 45, pp. 389–390, Apr. 9, 2009.

[22] M. Margadan-Mendez, A. Juslin, S. V. Nesterov, K. Kalliokoski, J. Knuuti, and U. Ruotsalainen, "ICA based automatic segmentation of dynamic (H2 O)-O-15 cardiac PET images," *IEEE Trans. Inform. Technol. Biomed.*, vol. 14, pp. 795–802, May 2010.

[23] X. Q. Dai, J. Tian, and Z. Chen, "An input function estimation method for dynamic mouse F-18-FDG microPET studies," in *Proc. IEEE Nul. Sci. Symp. Med. Imag. Conf.*, New York, NY, USA, 2011, pp. 3091–3096.

Authors' photographs and biographies not available at the time of publication.